A virtual anti-scatter grid for multi-energy photon counting detector systems

Zenith Purisha, Alexander Winkler, Muhammad Emzir,
Roland Hostettler, Panja Luukka, Simo Särkkä

DOI:

E10.1088/1402-4896/ad7ce1

A virtual anti-scatter grid for multi-energy photon counting detector systems

Zenith Purisha[1,4*], Alexander Winkler[2,3*], Muhammad Emzir[1,5], Roland Hostettler[1,6], Panja Luukka[2], Simo Särkkä[1]

[1]Department of Electrical Engineering and Automation, Aalto University, Finland
[2]Helsinki Institute of Physics, University of Helsinki, Finland
[3]Detection Technology Plc, Espoo, Finland
[4]Department of Mathematics, Universitas Gadjah Mada, Indonesia
[5]Department of Control and Instrumentation Engineering, King Fahd University of Petroleum and Minerals
[6]Department of Engineering Sciences, Uppsala University, Sweden
[*] *corresponding authors*

Abstract. Photon-counting (PC) systems are the next technological generation of medical computed tomography (CT) imaging and is being worked on by all major system providers. CT devices that are based on PC detectors enable multi-energy data collection. The information-content of this data can be used to obtain more detailed patient data, which improves the quality of reconstructions, compared to conventional detector systems. However, PC CT systems are subject to radiation scatter as just as any other imaging systems is. Conventionally anti-scatter grids (ASG) are used to reduce the scatter effect. These are however an imperfect solution, especially for PC detectors. In this work, a software-based scatter correction method, thus a virtual ASG is proposed. The method is tailoring a new statistical model in the measurement space and combining it with the statistical inversion method called Markov chain Monte Carlo (MCMC). The method can recover the measurement data from dense projections. We present the method on simulated data of a single photon emission computed tomography (SPECT) problem for which only under-sampled data is available. However, our approach can in principle be generalised to CT, PC-CT, Positron emission tomography (PET), radiotherapy, or even digital radiography problems. The results show that the proposed model performs similarly as physical ASGs and for cases where ASGs are not possible. The model further offers a significant improvement in the quality of the reconstruction image compared to the image reconstruction from original under-sampled data.

1. Introduction

Photon-counting (PC) computed tomography (CT) is favoured as the next step for clinical tomographic medical imaging and is being developed by major system providers, e.g. [1, 2, 3, 4], with recent FDA approval of the first PC systems for clinical usage [5].

In PC-CT, the energy of an incoming photon is evaluated on a per quanta basis, allowing to construct the spectrum of the images object by using several energy thresholds. This is also referred to as multi-energy CT [6, 7]. In contrast to conventional CT, the PC-CT offers several advantages. For example, increased contrast between different soft tissues, quantitative CT images using well-defined energies, K-edge contrast and reduced patient dose, if high-Z materials are being used [8, 9, 10, 11].

PC-CT however, faces a similar complication as other radiographic methods do, the inherent problem of radiation scattering. This is a physical process that inevitably occurs on all structures that the radiation is passing. In particular the patient and the detector itself. Furthermore, scatter effects are dependent on materials and atomic numbers of the elements involved [12]. From a detector point of view, the scattering of photons reduces the number of photons that travel in a direct path to the detector, while increases the number of photons that deviated from this direct path. For PC devices, additionally the energy of the direct path photons changes. As a consequence the image contrast is reduced. Anti-scatter grids (ASGs) or collimators (depending on the detector type and application) reduce this effect, by removing some of the deviated photons. This increases the relative contrast of the signal coming from the primary beam path. ASGs and collimators are however imperfect solutions, because a compensation for the removed photons is required, not all scattered photons can be removed and some of the remaining primary beam photons still have a changed energy spectrum. Even with dedicated ASGs, the amount of scattered radiation in CT is still around 17% [13] and about 21% in cone beam breast CT [14]. This is in addition to higher patient exposure, to compensate for the removed photons. Another downside of anti-scatter grids is their increasing cost-ineffectiveness, with decreasing pixel sizes. As the precise manufacture and assembly of expensive materials such as copper or tungsten is a tedious task [15] and effective scattered photon removal becomes more challenging with thinner wall thicknesses, that is required at small pixel sizes. A way to avoid these downsides, is to transfer the ASG functionality from the physical device into the (virtual) data space. Previous work of virtual scatter correction and kernel parametrization have been proposed for example by Ruhrnschopf et al. [16, 17] as and Star et al. [18, 19]. Those corrections however, are based on either time consuming Monte Carlo simulations [20] or methods that ignore the target's true geometry, such as kernel-based methods. The later rely on the smoothness of the scattered intensity. Even though, fast methods have been presented that improve contrast to a degree, they are inherently non-optimal solutions, as the scattered intensity is depending on the target and suffers in computing of the forward model, during reconstruction [19]. Additionally, the removed scattered radiation still needs to be compensated through higher photon flux and therefor patient dose.

Even though, the first PC-CT systems are now approved, the data availability is still rare [1, 2]. Thus, only a few studies have been performed on multi-scattering correction in PC-CT [21, 22]. Hence, there is room to investigate and develop the field of multi-scatter correcting for PC-CTs, in order to improve the contrast-to-noise ratios of

patient imaging [23]. A computationally fast and adaptive model that takes advantage of the additional informational dimension of PC detectors would be the preferred solution [17, 24, 25].

The problem of photon scatter and the subsequent image degradation is not limited to CT imaging only. For example, beam and patient positioning are essential for radiation therapies [26]. Although, direct patient dose is less of a concern for radiation therapies, the radiation scatter induced dose however is. The higher intensities of the radiation therapies create substantially larger amount of photon scatter, which in turn will affects dose or positioning calculations. An experimental therapy that requires dose calculations for its breakthrough is the Boron Neutron Capture Therapy (BNCT), which intends to use a Single Photon Emission Computed Tomography (SPECT) imaging geometry, to obtain tumor dose and therapy plan information. In this work, we focus on scatter correction in BNCT-SPECT problems. The presented corrections however, can be applied to other radiographic and radiotherapeutic methods as well, provided a PC detector is used. Unfortunately, specialized PC detectors for BNCT-SPECT do not exist yet either. However, various research groups are working on prototypes [27, 28, 29, 30]. These groups produce representative simulated data that can be utilized for the purpose of this paper.

In this work, we perform image reconstructions and a background substraction to reduce the scattering phenomena. We use analytical Radon transforms of ellipses to form the tomography model, in particular we model the PC-CT measurement of the Boron/tumor shape using a collection of ellipses. The parameters of this model are statistically estimated using Markov chain Monte Carlo [31, 32]. Various statistical methods have been previously developed and implemented in standard CT imaging [31, 33, 34]. In this paper, we combine our statistical model with PC-SPECT data (representing PC-CT data) using MCMC as a scattering correction method, with the aim to recover dense and full data sets from limited projections.

1.1. Boron Neutron Capture Therapy

Boron neutron capture therapy (BNCT) is a binary radiography for certain malignant tumors, especially in the head and neck region [35]. It has been evaluated since in various clinical trials e.g. by Savolainen et al. [36] or Barth et al. [37]. In order for this therapy to gain general acceptance, real time patient dose calculations are required [30]. The most favoured approach to perform this, is prompt-gamma (PG) imaging of the boron neutron capture reaction, which creates the therapeutic effect [30]. PG imaging in BNCT is in principle similar to SPECT [38, 39] and is therefor called BNCT-SPECT [40]. The main complication is that the PG signal that allows to determine the dose, is small compared to the background signal [40]. This further complicates the inherent scatter problem of the SPECT like setup.

The main difficulty of PG imaging in BNCT is the small signal amplitude in comparison to the background and neutron induced background [30]. Integrated signal

count-rates of a few 10s of counts per second (cps) can be expected by typical ^{10}B concentrations of approximately 50 ppm during the therapy. The PG from the boron neutron capture reaction (BNC) are emitted isotropic. Thus, the number of photons reaching a detector, which can only cover a portion of the solid angle is small compared to the approximately 10^7 neutrons/ cm^{2}s, that are also reaching a detector at the same time [30]. In addition to this main difficulty, is the PG signal from the BNC reaction also affected by scattering. From the imaging point of view, is the already small signal contrast further reduced by scatter effects. ASGs, or collimators are non-feasible solutions in BNCT-SPECT, due to the small signal amplitude and the additional secondary scatter effects that are caused by the ASG itself, when interacting with the neutron field. The latter can cause significant additional out of tumor dose to the patient.

Fortunately, the neutron background can also be used for the patient dose calculations as proposed in [41]. In this case, no neutron ASGs would be required. These however are complex and bulky structures, which are unfeasible for patient imaging devices and create yet again additional patient dose. Therefore, neutron ASGs are not feasible for the therapy. BNCT-SPECT was chosen as an example to present our virtual ASG solution as it allows to demonstrate the functionality on both photon and particle (here neutron) data simultaneously.

2. Parameter estimation for BNCT-SPECT problem

In this section the aim is to describe our approach to solve the scatter problem, which is based on modeling the object using simple circular primitives in order to make computations tractable. This requires a parameter estimation of the relevant variables as well as various simplification, which are described in this section.

2.1. Measurement model

For the described problem, we use the number of the BNC reaction photons, as registered by the detector and after background subtraction. In detail, the detector registers a full beam spectrum in each pixel and all but the 478 keV photons are removed from the spectra of each pixel, which is essentially a digital spectral filter. The remaining data can be considered to be virtual monochromatic. Scatter effects cause a Gaussian distribution of the 478 keV photons around the center of the boron target, which is registered accordingly by the detector pixels. The full beam spectrum consists of the primary beam photon spectrum, secondary photons from neutron interactions in the phantom and the detector, as well as inelastic scattered photons. A schematic representation of the setup, the full beam spectrum with the BNC signal is presented in Figure 1 and Figure 2. Details about the phantom and the tumor insert have been described in [30]. The usage of a PC detector is a key property to make our approach possible. It enables digital filters, to extract the signal of interest from the spectrum of each pixel (BNC

reaction peak at 478 keV), without interference from neighbouring peaks such as the annihilation peak at 511 keV. Our goal is to estimate the location and distribution of the BNC signal a patient or patient phantom. In context of this problem, we model the tumor and the BNC distributions to be circles or ellipses. Thus we will represent the reconstruction of the tumor images in terms of ellipses as well. The term *boron* will be used as synonym for BNC signal or boron signal within this work.

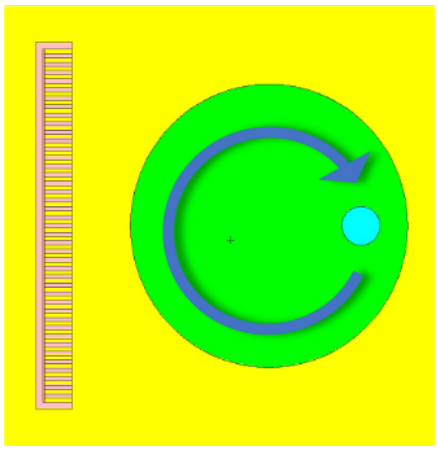

Figure 1. The setup that has been simulated. Left: detector with ASG grid, Center: phantom with tumor insert and arrow indicating rotation.

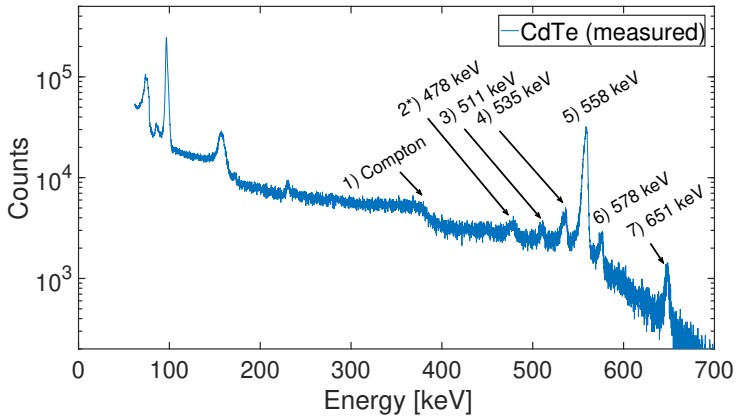

Figure 2. Full spectrum that was simulated for the various setups in this work. A spectrum as this was received in every pixel. The peak number 2*) is the BNC signal, whilst the rest of the spectrum is considered background signal.

We can compute the Radon transform of an ellipse in closed form. Consider an ellipse v with center at (x_c, y_c) with major axis a and minor axis b with angle ϕ. Assume

that the ellipse has only one attenuation value g (a homogeneous ellipse). This case represents a single primary tumor in a patient and is a simplified case of the therapy. Analytically, the Radon transform $R_{r,\theta}$ for this ellipse at given p' and θ is written in a closed form following a similar calculation in [42]:

$$R_{r,\theta}v = gL_{r,\theta}v, \tag{1}$$

where

$$\begin{aligned} L_{r,\theta}v &= 2a\frac{\zeta}{\xi}, \\ \zeta^2 &= a^2 + b^2 + \cos^4(\theta-\phi) + b^4\sin^4(\theta-\phi) - b^2d^2, \\ &\quad + b^2(a^2+b^2)\sin(\theta-\phi)\cos^2(\theta-\phi), \\ \xi &= a^2 + \cos^2(\theta-\phi) + b^2\sin^2(\theta-\phi), \\ d &= -r + x_c\cos(\theta) - y_c\sin(\theta). \end{aligned} \tag{2}$$

For an ellipse v, $L_{r,\theta}v$ represents the length between two points where the Radon line parameterized with r, θ intersect the ellipse with attenuation value g.

We will assume that the image, which in this case is the the boron distribution, for simplicity in the computational algorithm, only has one circle as written in (3) such that

$$\begin{aligned} \zeta^2 &= 2a^2 + \cos^4(\theta-\phi) + a^4\sin^4(\theta-\phi) - a^2d^2, \\ &\quad + 2a^4\sin(\theta-\phi)\cos^2(\theta-\phi), \\ \xi &= a^2 + \cos^2(\theta-\phi) + a^2\sin^2(\theta-\phi), \\ d &= -r + x_c\cos(\theta) - y_c\sin(\theta). \end{aligned} \tag{3}$$

and the parameter ϕ is fixed. This is based on the assumption that the BNC reaction occurs mainly in the tumor area, in which the concentration of the radiopharmaceutical is highest during the therapy. However, the proposed model can be applied for different shape of tumor by approximating it using several ellipses which means more parameters are required.

2.2. Statistical model

In this work, we use a statistical model to estimate the parameters in (3) [43, 34]. The measurement of the boron distribution can be modelled as follows:

$$\mathbf{m} = R_{r,\theta}v + \varepsilon, \tag{4}$$

where ε is the measurement noise and it is normal distributed $\varepsilon \propto \mathcal{N}(0, \sigma_\varepsilon^2 I)$, where I is an identity matrix. In this discussion, we consider a linear measurement model with additive Gaussian errors.

The likelihood function corresponding to (4) is:

$$p(\mathbf{m}|x_c, y_c, a, b, g) \propto \exp\left(-\frac{1}{2\sigma_i^2}\|R_{r,\theta}v - \mathbf{m}\|^2\right), \tag{5}$$

where $\mathbf{m}$ is the pre-processed measurement data which will be discussed in Section 2.3. Since we assume that the tumor is only a circle, then parameter a equals to b.

Hence, the posterior distribution of parameters can now be written as follows:

$$p(x_c, y_c, a, g|\mathbf{m}) \propto p(\mathbf{m}|x_c, y_c, a, g)p(x_c)p(y_c)p(a)p(g), \tag{6}$$

where a Gaussian prior for each parameter is used. In this article we use a Markov chain Monte Carlo (MCMC) method is to estimate the parameters. MCMC is one of the most popular techniques for sampling from probability distributions, and is based on the construction of a Markov chain that has the desired distribution as its equilibrium distribution [31]. The basics idea of Monte Carlo integration is to generate samples $\mathbb{X} = \{x_c^{(\ell)}, y_c^{(\ell)}, a^{(\ell)}, g^{(\ell)} : \ell = 1, \ldots, L\}$ from $p(x_c, y_c, a, g|\mathbf{m})$ [31, 32]. The goal is to estimate parameters x_c, y_c, a, and g in order to recover the limited measurement data to be complete data sets from dense angles. The Metropolis–Hastings algorithm (see, e.g., [32]) is employed to sample from the posterior distribution (6). The algorithm for sampling the vectors $\mathbf{x} = (x_c, y_c, a, g)$ has the following steps:

(i) Initialize value $\mathbf{x}^{(\ell)} \in \mathbb{R}^4$, and set $\ell = 1$.

(ii) Draw $\mathbf{y} \in \mathbb{R}^4$ from a proposal distribution $q(\mathbf{x}^{(\ell)}, \mathbf{y})$ and calculate the acceptance ratio

$$\alpha(\mathbf{x}^{(\ell)}, \mathbf{y}) = \min\left\{1, \frac{p(\mathbf{y})q(\mathbf{y}, \mathbf{x}^{(\ell)})}{p(\mathbf{x}^{(\ell)})q(\mathbf{x}^{(\ell)}, \mathbf{y})}\right\}.$$

(iii) Draw $t \in [0, 1]$ from uniform probability density.

(iv) If $\alpha(\mathbf{x}^{(\ell)}, \mathbf{y}) \geq t$, accept the candidate by setting $\mathbf{x}^{(\ell+1)} = \mathbf{y}$, else $\mathbf{x}^{(\ell+1)} = \mathbf{x}^{(\ell)}$.

(v) If $\ell = L$ (number of iterations) then stop, else set $\ell = \ell + 1$ and return to step 2.

We use a point estimate, that is a conditional mean (CM) estimate for parameters $\mathbf{x}$, and it can be written as follows:

$$\mathbf{x}^{\mathrm{CM}} \approx \frac{1}{\widetilde{L}} \sum_{\ell=L_0+1}^{L_0+\widetilde{L}} \mathbf{x}^{(\ell)}, \tag{7}$$

where the first L_0 samples (the burn-in) are discarded.

2.3. Data sets pre-processing

In this work, the focus is on the BNCT-SPECT problem, with data collected on a head-phantom. The main interest lays in observing the BNC signal that originates from the tumor inside the phantom. However, the signal coming from the phantom contains both BNC and a wide spectrum of other signals. The latter is in this work referred to as background signal. Henceforth, a background subtraction is required and it is carried out as follows:

(i) A phantom which represents a patient's head is imaged once. It is then referred to as background data. During therapy this could be obtained through a prior (PC) CT scan. Figure 1 and Figure 2 present the simulated geometry and an example spectra that was received in each pixel. Details, such as size and material of the phantom and tumor insert have been reported earlier [30]. The peaks number 2*) and 5) are the BNC and CdNC signals, respectively and are extracted from the spectra of each pixel. The rest of the spectra of each pixel is considered background in this work. Such spectra, albeit significantly lower energy resolution, can be obtained by photon counting CTs, or CBCTs. For radiation therapies, this data could be obtained with the kV or MV imaging systems that are used for scouting and verification of the therapy status, provided that the detectors of these systems are PC detectors with an energy resolution per pixel similar to what is presented in this work. These imaging systems also in sparse imaging mode, which is a scenario similar to what is presented here.

(ii) A tumor insert is placed in the phantom and projection data is collected. This represents the imaging data collected during the therapy. In this meaning, for each scenario presented in this work, two data sets were simulated. With the difference that one of them had a tumor insert (blue circle on the right side of Figure 1) and the other one did not.

(iii) The data sets obtained in step (i) are subtracted with a scaling factor from the image data of step (ii). The factor compensates the image intensity differences between the CT scan and the BNCT-SPECT data. For this work, the scaling factor is found empirically. In future work, this factor should be obtained based on reliable references, this however requires dedicated research and is left out of the scope from this work. One option would be to use peaks of the spectrum that are not related to the reactions in the phantom or the tumor inserts, for example. The peak at approximately 250 keV in Figure 2 could be a candidate.

(iv) The BNC signal is extracted from the data set by digital filtering. Thus, selecting the energy bin of the PC detector that is set around the BNC reaction peak.

The discussion of this work focuses on the application of the presented algorithm to the data sets obtained from step (iv).

3. Experimental description

3.1. Data generation

Our simulated experimental setup consists of a poly methyl-methacrylate (PMMA) phantom, that is representing a patient's head. A circle shaped tumor inserts are added to the phantom as it is shown in Figures 1 and 3. The simulations were performed in MCNP5 version 1.4, the epithermal neutron beam model of FiR 1 described by Seppälä [44] and the nuclear data library TENDL-2008-ACE, provided by the Nuclear Energy Agency [45] were used [46]. The phantom is imaged with a PC line detector in 32 angles,

covering a full rotation. The imaging process of the phantom with the tumor insert takes place during the irradiation and represents the real time imaging of the patient tumor during the therapy session.

The PC detector consists of 42 pixels, each recording a full spectrum between 100 and 800 keV and with an energy resolution of approximately 6 keV at 662 keV (1 %, ^{137}Cs calibration reference), as reported in [30]. The pixels are modelled as natural CdTe crystals of $3\,\mathrm{x}\,3\,\mathrm{x}\,1\,\mathrm{mm}^3$ size. At this thickness, the detector can provide reasonable statistics of a few 10s of counts, up until 800 keV, while being transparent to higher energetic photons, as described in [41] and [30]. Furthermore, the simulated data is corrupted by scattering processes and the sparse rotational angle problem (only 32 rotations, each 11.25° apart). With this condition, several data sets were simulated to evaluate the effect of our spectral reconstruction algorithm. For the first set (ASG), a detector with pixels separated by $3\,\mathrm{x}\,22\,\mathrm{mm}^2$ lead (Pb) walls was simulated, as presented in Figures 1. These were removed for the second data set ($non - ASG$). Finally, the third data set ($noise-test$) is similar to the second one, however the BNC (and neutron) signal strengths were reduced to the noise floor of the background data set. We use this third data set to check if the algorithm will fail, if the input data has no feasible signal to reconstruct. Since each data set contains a full set of spectra for each pixel, the neutron signal can be extracted with the same processes as the boron signal, albeit at a different energy (558 keV, peak number 5) of Figures 2). The process has been described in [41]. The signal type used for each data set is indicated by the subscripts $_{BNC}$ and $_{CdNC}$ for the boron and neutron signal, respectively. In all cases simulations were performed until the statistical variance reached 5 % or less and a Hamming filter was used for all FPBs reported in this work. The tumor insert (yellow circle) of Figure 3 presents the ground truth that we intend to reconstruct. The corresponding sinogram and FBP, are a single sinewave and a circle of the size and position as the yellow insert. We refrain from presenting sinogram and FBP of the tumor insert here, however Figure 5(a) and (c), principally depict the ground truth dataset.

4. Results and Discussion

4.1. Boron signal reconstruction

In this work, the proposed parameter estimation method is implemented to compute the reconstruction image from the BNC signal, *i.e.* SPECT data sets or *sinogram* of photons that are captured by the detector, originating from the BNC reaction. The subtraction of the backgrund signal is carried out during pre-processing of the sinograms and we assume that the boron in the tumor is distributed homogeneously over one small area only. Thus, it will correspond to a single sine curve-like shape in the sinogram. However, in this problem we deal with under-sampled data sets, particularly, only limited angle data sets are available [43]. This occurs in addition, to the sparse distribution of data set itself. Data sets recorded of such cases are only a part of a 'sine-curve' as shown in Figure 4(a).

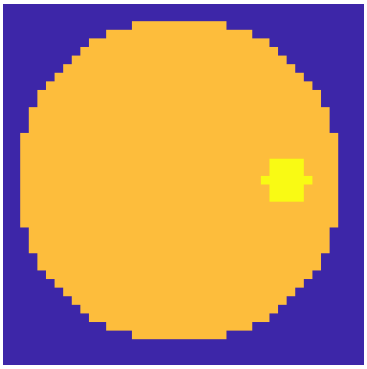

Figure 3. PMMA phantom to represent a patient's head with a tumor inserted.

Furthermore, the under-sampled signal is broadened by photon scattering. Figure 4(c) illustrates this with a blurred and boarder partial sine curve, spanning approximately 12 projection angles. This scatter broadened signal shows furthermore higher intensities (maximum signal value in a.u.) than the non-broadened signal, see Figure 4(c) versus (a), where the yellow signal spans approximately 12 projection angles. This difference originated from the removed photons by the ASG (Pb walls). The corresponding FBP are presented in the panels (b) and (d) of Figure 4. Please note that maximum intensity of the FBP is lower for the $non - ASG_{BNC}$ data set, despite the signal being larger than for the ASG_{BNC} data set. Furthermore, please note that the image size changes after reconstruction by the FBP, leading do different number of pixels between singogram and FBP images. Finally, the phantom (large green circle Figure 1, or large orange circle Figure 3) is not visible in Figures 4, 5, 9 - 11 as the corresponding signals have been filtered out during data pre-processing (see section 2.3).

The proposed method was then applied to both data sets, in order to recover the dense projection data from the limited and sparse angle data sets and to reduce the scatter effect. The result of the estimated sinogram and the corresponding FBP reconstruction are presented in Figure 5(a) for the scatter free (ASG_{BNC}) and scatter distorted ($non - ASG_{BNC}$) data sets Figure 5(c), respectively. It can be seen, that the proposed method is able to recover the information from the missing projection angles, resulting in a full recovered sinogram with dense angles. The method also reduced the scatter effects significantly, by focusing the signal on approximately 7 projections angles only, Figure 5(c). The corresponding FBP (Figure 5(d)) present a decent reconstruction of the recovered signals, which is in case of the ASG_{BNC} data set a significant improvement compared to Figure 4(d). The intensity has increases for both sinograms, which can be attributed towards the more focused sinogram and significantly reduced background. Finally, the completely recovered sinograms result in

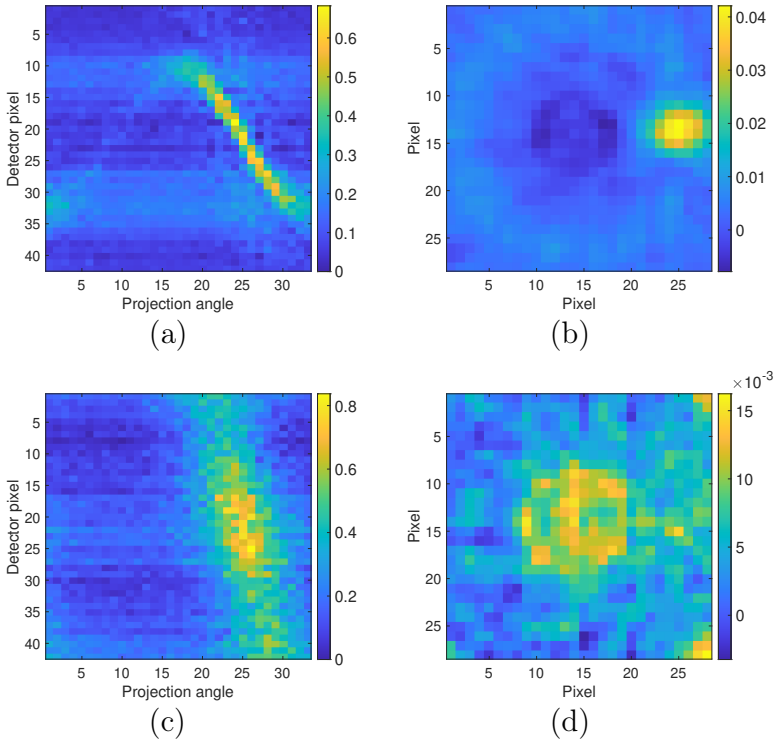

Figure 4. (a): Sinogram of the under-sampled boron signal (data set ASG_{BNC}) without scatter effects. (b): FBP of the sinogram in (a). (c): Sinogram of the under-sampled boron signal with scatter effects (data set $non - ASG_{BNC}$). (d): FBP of the sinogram in (c). The FBP fails due to scatter distorted and incomplete data. Please note that the phantom (large green circle Figure 1, or large orange circle Figure 3) is not visible in these images, as the corresponding signals have been filtered out during data pre-processing (see section).

a focused and more intense FBPs. The reconstructed tumor (Figure 5(c)) does change in size, compared to the reconstruction of Figure 5(d). This is due to the less focused sinogram produced by the proposed method.

Table 1. The parameter estimates from data set ASG_{BNC} which calculated using the conditional mean. The SD values are also reported in parentheses.

Parameters	x_c (SD)	y_c (SD)	a (SD)	g (SD)
Value	0.293 ($3.35.10^{-2}$)	0.290 ($1.34.10^{-2}$)	0.085 ($5.3.10^{-3}$)	5.47 (1.48)

The Metropolis–Hastings algorithm took 50 000 samples in total, while half of samples were used for the *burn-in* period [32]. The MCMC samples are well-mixed and marginal distributions of each parameters as they are presented in Figure 6 and 8. It means the samples moves throughly the posterior distribution. It also follows by the parameter estimated which calculated using the conditional mean as it is written in (7)

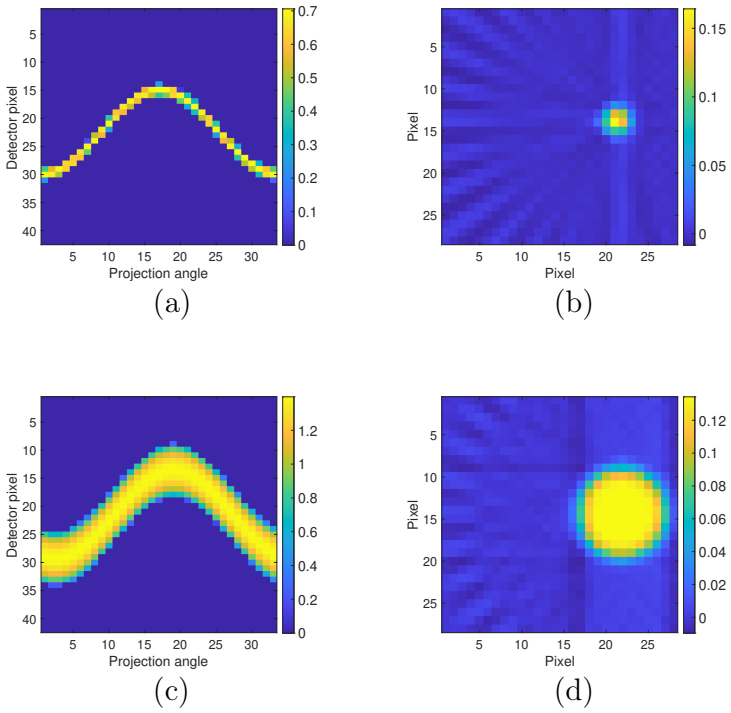

Figure 5. (a): Reconstructed sinogram from scatter free BNC signals of data set ASG_{BNC}. (b): FBP of the reconstructed sinogram in (a). (c): Reconstructed sinogram from scatter distorted BNC signals of data set $non - ASG_{BNC}$. (d): FBP of the reconstructed sinogram in (c), is successful due to scatter free and completed data.

Table 2. The parameter estimates from data set $non - ASG_{BNC}$ which calculated using the conditional mean. The SD values are also reported in parentheses.

Parameters	x_c (SD)	y_c (SD)	a (SD)	g (SD)
Value	0.34 ($1.9..10^{-2}$)	0.29 ($1.8.10^{-2}$)	0.15 ($3.1.10^{-3}$)	5.34 (0.44)

and reported in Table 2.

The proposed method took around 9 seconds to complete. It is computed using MATLAB 2018a with 2,3 GHz Intel Core i5 in memory 8 GB. The computation time of the proposed method can be considered as a fast algorithm even though MCMC is applied. This is due to the parameterized model which can reduce the dimension of the target of interest. In addition, the sinogram obtained by the proposed method is not limited to the resolution image of the original data sets.

4.2. Reconstruction of the noise-test data set

The FBP of the $noise - test_{BNC}$ fails as expected, see Figure 9(a) and (b). A partial sinogram is reconstructed from the noise data. Based on the input data this is not

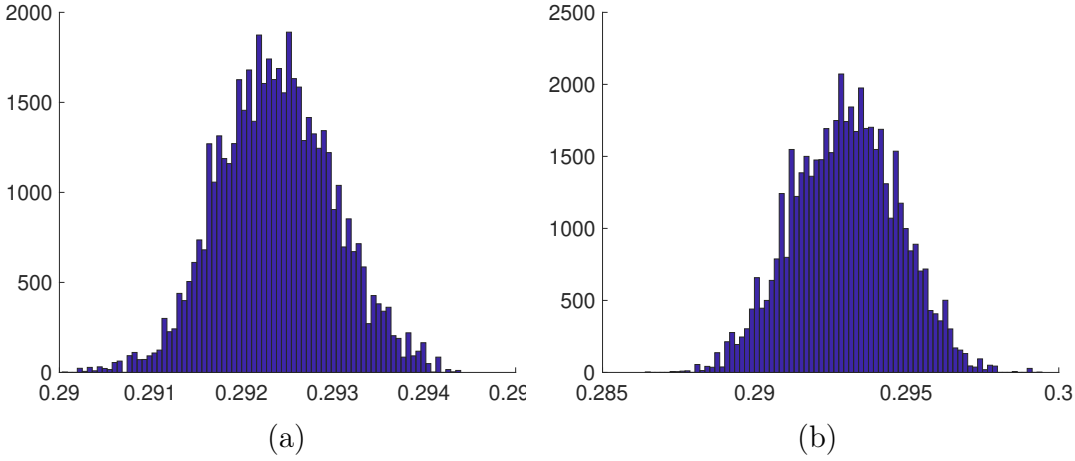

Figure 6. (a) and (b): Marginal distribution of parameter sample x_c and y_c for the data set ASG_{BNC}, after *burn-in* period, respectively.

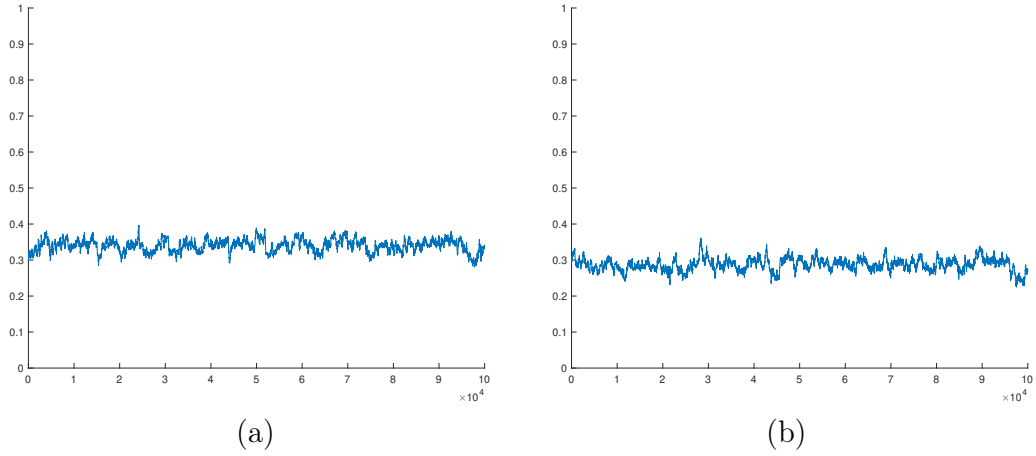

Figure 7. (a) and (b): The Markov chain Monte Carlo chains of x_c and y_c for the data set ASG_{BNC}

expected, however also not impossible. As the boron signal was reduced to the noise floor. Thus, there is a possibility given, that a few projections contain a signal slightly larger than the background that the algorithm was able to reconstruct, Figure 9(c). Due to the partial sinogram and constant background of the reconstruction, the FBP succeeds to construct an object at the tumor location. However, distorted and at significant smaller size than the actual tumor insert. This leads to the hypothesis that the algorithm blindly constructs a signal, even if there is none. This would be devastating for an application such as the boron dose calculation for BNCT. When inspecting the intensities of the input and reconstructed sinograms, it is obvious that the $noise - test_{BNC}$ and the reconstruction signals are respectively 10^4 and 10 times

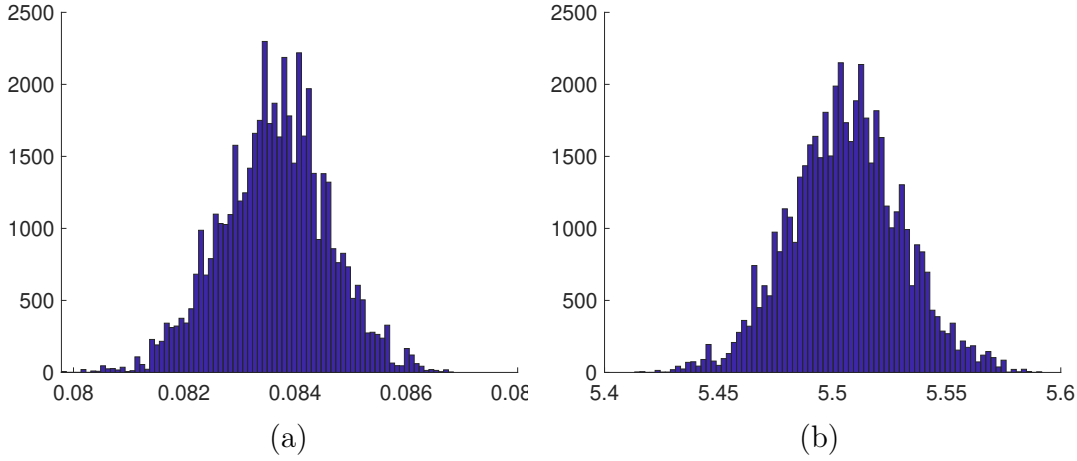

Figure 8. (a) and (b): Marginal distribution of parameter sample a and g for the data set ASG_{BNC}, after *burn-in* period, respectively.

smaller than the corresponding $non - ASG_{BNC}$ signals. See panels (a) and (c) of Figure 5 and Figure 9. A similar situation occurs for the FPBs, panels (b) and (d) of the respected figures. This allows to use a simple threshold filter and abort the algorithm if the reconstructed sinograms and FBPs are below a certain threshold. Arguably, more sophisticated rejection algorithms can be used. These however go beyond the scope of this work.

In summary we showed that the tumor image, based on the boron signal, is well reconstructed and not dominated by artefacts as the limited angle and scatter distorted $non - ASG_{BNC}$ image is. As the method proposed, the sinogram is reconstructed so that it covers for all projection data. Applying the algorithm on a noise data set ($noise - test_{BNC}$) results in a partial sinogram reconstruction at considerably reduced intensity. Such reconstructions can be rejected through thresholds or advanced rejection algorithms.

The MCMC chains of x_c and y_c reported in Figure 7 seem to be mixing very well. The convergence determined by visually looking at chain plots and also by Geweke's convergence diagnostic[47]. The Geweke's statistics give result less than 0.0075 in an absolute value term. It can also be seen in Figure 6 that all marginal distributions are unimodal which indicate that the chain converge to the target distribution. In this work, the computation time takes less than one minute. For complex structures that need many ellipses and circles, the computation surely will take longer. The algorithm can be sped-up by tuning the covariance function adaptively [48, 49].

4.3. Neutron signal and noise-test

From the algorithm point of view it does not matter what is the source of the signal, as long as part of a sinogram present in the data. Therefore, we applied the algorithm to

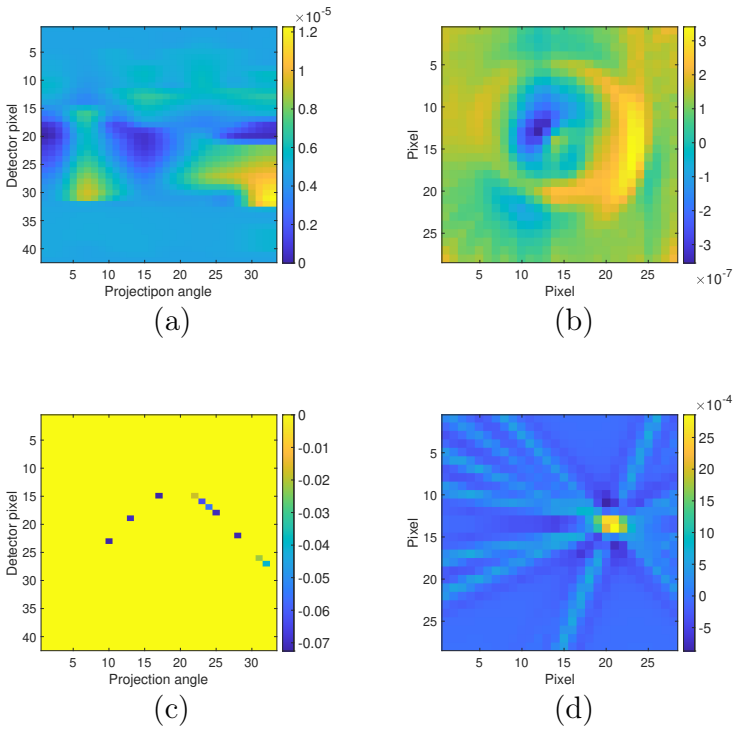

Figure 9. (a): Sinogram from $noise - test_{BNC}$ data with scatter distortion. (b): FBP of the sinogram in (a). (c): Reconstruction of the sinogram in (a), a partial sine curve is found. (d): FBP of the reconstructed sinogram in (c), succeeds to produce an object at the tumor location.

the $non - ASG_{CdNC}$ data set. Please note that in case of the neutrons, the sinogram and FBP of the raw signals is nearly identical for the ASG_{CdNC} and $non - ASG_{CdNC}$ data sets. This is caused by the negligible neutron scatter cross section of Pb. Hence, the Pb walls that act as ASG for the photons, are transparent for neutrons. Nonetheless, neutrons scatter heavily on selected elements such as hydrogen. Hydrogen being the most common element, results in a heavily scatter distorted neutron signal by default. The Figure 10 presents the sinograms and corresponding FBPs of the scatter distorted neutron and reconstructed data ($non - ASG_{CdNC}$ set), respectively.

Table 1 and Table 2 shows that the conditional mean of x_c, y_c and g for ASG_{BNC} and $non - ASG_{BNC}$ are not significantly different. However, the estimated parameter a for $non - ASG_{BNC}$ is almost twice as it in the ASG_{BNC}. This is due to the scatter distorted data sets. It is visible that the algorithm performs similarly as for the scatter distorted photon data set. A full sinogram is produced and the FPB shows a tumor target at the location of the actual tumor insert. The intensities of the sinograms are approximately 5 times larger than the intensities of the corresponding boron images, while the intensity of the FBP is approximately 3 times larger than the respected FBP of the $non - ASG_{BNC}$ data set. Such larger intensities may allow to reconstruct a tumor in BNCT, even if the boron signal is too small for a successful reconstruction. In such

cases the neutron signal is expected to be still measurable, as described in [30].

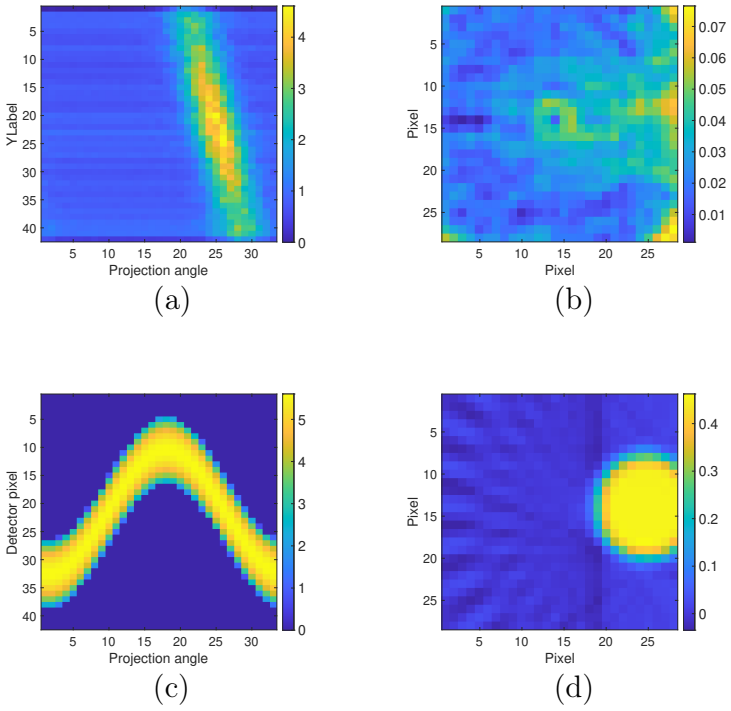

Figure 10. (a): Reconstructed sinogram from scatter distorted neutron signals of data set $non - ASG_{CdNC}$. (b): FBP of the reconstructed sinogram in (a). (c): Reconstructed sinogram from data presented in (a). (d): FBP of the reconstructed sinogram in (c), is successful due to scatter free and completed data.

We have performed the noise test for the $non - ASG_{CdNC}$ data set as well, in case the neutron signal is also below the noise floor. Hence, an artificial but realistic $noise - test_{CdNC}$ data set was created and the algorithm applied. The reconstruction is presented in Figure 11) and produced similar results as for the $noise - test_{BNC}$ data set (see Figure 9). The sinogram in Figure 11)(a) shows indication for a partial sine curve. This might be the case for a real measurement, as the neutron signal is substantially larger than the boron signal[30]. Nonetheless, the intensity is too low and coincidence of noise signals cannot be ruled out. The FBP of the initial sinogram fails as expected, see Figure 11(b) and the reconstruction of the sinogram still produces a partial since curve (c). Finally, the FBP of the reconstructed sinogram produces an object again at the tumor location, however at an intensity approximately 100 x smaller than the object in Figure 10(d). Therefore, these results can also be rejected through a threshold application.

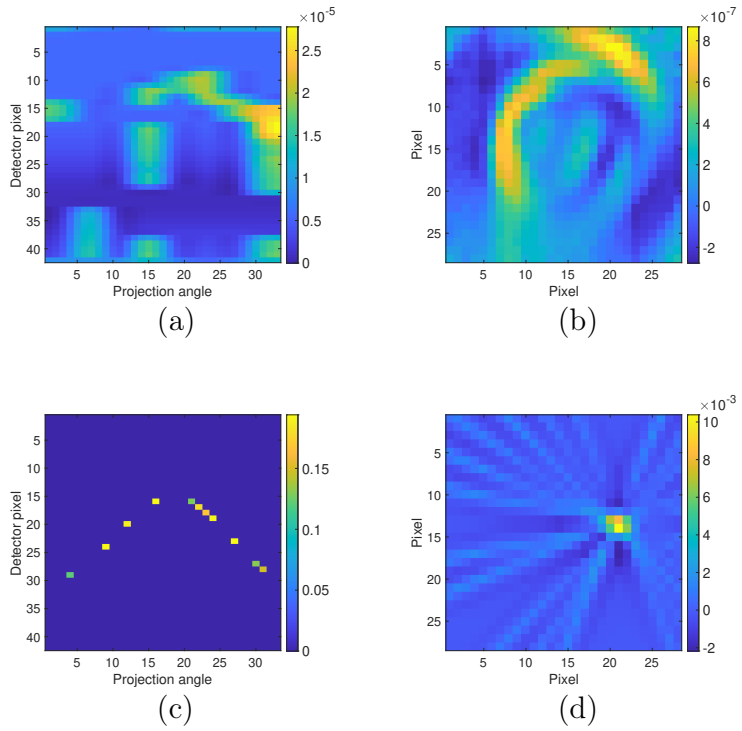

Figure 11. (a): Sinogram from $noise - test_{CdNC}$ data with scatter distortion. An indication of a sine curve is visible. (b): FBP of the sinogram in (a). (c): Reconstruction of the sinogram in (a), a nearly complete sine curve is found, which is due to larger neutron signal, compared to the boron signal. (d): FBP of the reconstructed sinogram in (c), succeeds to produce an object near the tumor location. Albeit, too smaller and low intensity.

5. Conclusion

We have presented a scattering correction method for under-sampled data for photon-counting systems using a statistical model combining with an MCMC-based parameter estimation method. This approach is to approximate the anti-scatter grid functionality for scattered distorted signals such as the photon and neutron signals in BNCT, if the signals are digitally filtered as it is possible with spectral data obtained from photon-counting detectors. The algorithm succeeded to reconstruct the signals at the correct positions, despite an overwhelming noise background in each data set and acts as a virtual anti-scatter grid. This allows to measure, even in difficult applications such as BNCT-SPECT, essential signals without the need of anti-scatter grids. The algorithm has also proven to be indifferent about the signal source, thus allowing it to be applied a wide range of data or signals, as long as the data is presented in form of a numerical array. With this work, we have shown to reproduce one object. The next step is to test the algorithm on data that is to be collected at a real BNCT facility in Helsinki, Finland as well as on data of multiple targets. Another outlook is to reconstruct an

arbitrary shape of tumor by approximating it using several ellipses. In addition, adding a scaling factor corresponds to the intensity value in the reconstructed image is possible to conduct in the future.

Acknowledgements
Authors acknowledge support from the Academy of Finland (314473, 314474, 313708)

References

[1] David P. Cormode, Salim Si-Mohamed, Daniel Bar-Ness, Monica Sigovan, Pratap C. Naha, Joelle Balegamire, Franck Lavenne, Philippe Coulon, Ewald Roessl, Matthias Bartels, Michal Rokni, Ira Blevis, Loic Boussel, and Philippe Douek. Multicolor spectral photon-counting computed tomography: in vivo dual contrast imaging with a high count rate scanner. Scientific Reports, 7(1), July 2017. doi: 10.1038/s41598-017-04659-9. URL https://doi.org/10.1038/s41598-017-04659-9.

[2] Rolf Symons, Bernhard Krauss, Pooyan Sahbaee, Tyler E. Cork, Manu N. Lakshmanan, David A. Bluemke, and Amir Pourmorteza. Photon-counting ct for simultaneous imaging of multiple contrast agents in the abdomen: An in vivo study. Medical Physics, 44(10):5120–5127, 2017. doi: 10.1002/mp.12301. URL https://aapm.onlinelibrary.wiley.com/doi/abs/10.1002/mp.12301.

[3] Mats Danielsson, Mats Persson, and Martin Sjölin. Photon-counting x-ray detectors for ct. Physics in Medicine & Biology, 66(3):03TR01, 2021.

[4] Bjoern Kreisler. Photon counting detectors: Concept, technical challenges, and clinical outlook. European Journal of Radiology, 149:110229, 2022.

[5] FDA Press release for photon counting CT. https://www.fda.gov/news-events/press-announcements/fda-clears-first-major-imaging-device-advancement-computed-tomography-nearly-decade, 2021. Accessed: 2021-11-14.

[6] N. G. Anderson, A. P. Butler, N. J. A. Scott, N. J. Cook, J. S. Butzer, N. Schleich, M. Firsching, R. Grasset, N. de Ruiter, M. Campbell, and P. H. Butler. Spectroscopic (multi-energy) ct distinguishes iodine and barium contrast material in mice. European Radiology, 20(9):2126–2134, Sep 2010. ISSN 1432-1084. doi: 10.1007/s00330-010-1768-9. URL https://doi.org/10.1007/s00330-010-1768-9.

[7] Salim Aymeric Si-Mohamed, Jade Miailhes, Pierre-Antoine Rodesch, Sara Boccalini, Hugo Lacombe, Valérie Leitman, Vincent Cottin, Loic Boussel, and Philippe Douek. Spectral photon-counting ct technology in chest imaging. Journal of Clinical Medicine, 10(24):5757, 2021.

[8] Katsuyuki Taguchi and Jan S Iwanczyk. Vision 20/20: Single photon counting x-ray detectors in medical imaging. Medical physics, 40(10), 2013.

[9] Martin J Willemink, Mats Persson, Amir Pourmorteza, Norbert J Pelc, and Dominik Fleischmann. Photon-counting CT: technical principles and clinical prospects. Radiology, 289(2):293–312, 2018.

[10] E Roessl and R Proksa. K-edge imaging in x-ray computed tomography using multi-bin photon counting detectors. Physics in Medicine and Biology, 52(15):4679–4696, July 2007. doi: 10.1088/0031-9155/52/15/020. URL https://doi.org/10.1088/0031-9155/52/15/020.

[11] Carsten O. Schirra, Bernhard Brendel, Mark A. Anastasio, and Ewald Roessl. Spectral CT: a technology primer for contrast agent development. Contrast Media & Molecular Imaging, 9(1):62–70, January 2014. doi: 10.1002/cmmi.1573. URL https://doi.org/10.1002/cmmi.1573.

[12] Katsuyuki Taguchi. Energy-sensitive photon counting detector-based x-ray computed tomography. Radiological Physics and Technology, 10(1):8–22, Mar 2017. ISSN 1865-0341. doi: 10.1007/s12194-017-0390-9. URL https://doi.org/10.1007/s12194-017-0390-9.

[13] Masahiro Endo, Shinichiro Mori, Takanori Tsunoo, and Hiroaki Miyazaki. Magnitude and effects of x-ray scatter in a 256-slice CT scanner. Medical Physics, 33(9):3359–3368, August 2006. doi: 10.1118/1.2239366. URL https://doi.org/10.1118/1.2239366.

[14] Xinming Liu, Chris C. Shaw, Tianpeng Wang, Lingyun Chen, Mustafa C. Altunbas, and S. Cheenu Kappadath. An accurate scatter measurement and correction technique for cone beam breast CT imaging using scanning sampled measurement (SSM)technique. In Michael J. Flynn and Jiang Hsieh, editors, Medical Imaging 2006: Physics of Medical Imaging. SPIE, March 2006. doi: 10.1117/12.656655. URL https://doi.org/10.1117/12.656655.

[15] Olga V. Makarova, Guohua Yang, Platte T. Amstutz, and Cha-Mei Tang. Fabrication of antiscatter grids and collimators for x-ray and gamma-ray imaging by lithography and electroforming. Microsystem Technologies, 14(9):1613–1619, Oct 2008. ISSN 1432-1858. doi: 10.1007/s00542-008-0558-7. URL https://doi.org/10.1007/s00542-008-0558-7.

[16] Ernst-Peter Rührnschopf and Klaus Klingenbeck. A general framework and review of scatter correction methods in x-ray cone-beam computerized tomography. part 1: Scatter compensation approaches. Medical physics, 38(7):4296–4311, 2011.

[17] Ernst-Peter Rührnschopf and and Klaus Klingenbeck. A general framework and review of scatter correction methods in cone beam ct. part 2: scatter estimation approaches. Medical physics, 38(9):5186–5199, 2011.

[18] Adam Wang, Edward Shapiro, Sungwon Yoon, Arundhuti Ganguly, Cesar Proano, Rick Colbeth, Erkki Lehto, and Josh Star-Lack. Asymmetric scatter kernels for software-based scatter correction of gridless mammography. In Medical Imaging 2015: Physics of Medical Imaging, volume 9412, page 94121I. International Society for Optics and Photonics, 2015.

[19] Josh Star-Lack, Mingshan Sun, Anders Kaestner, Rene Hassanein, Gary Virshup, Timo Berkus, and Markus Oelhafen. Efficient scatter correction using asymmetric kernels. In Medical Imaging 2009: Physics of Medical Imaging, volume 7258, page 72581Z. International Society for Optics and Photonics, 2009.

[20] Jian Yang, Yang Wang, Wei Zhou, Xianliang Jin, Yan Peng, and Jun Luo. A simple monte carlo model for performance optimization of single photon avalanche diode. Physica Scripta, 98(12):125503, 2023.

[21] Xiaohui Zhan, Kevin Zimmerman, Liang Cai, Xiaochun Lai, Madhuri Kaul, and Richard Thompson. Simulation of scattered radiation with various anti-scatter grid designs in a photon counting ct. In Medical Imaging 2019: Physics of Medical Imaging, volume 10948, page 109484Q. International Society for Optics and Photonics, 2019.

[22] A Sossin, V Rebuffel, J Tabary, Jean Michel Létang, N Freud, and L Verger. A novel scatter separation method for multi-energy x-ray imaging. Physics in Medicine & Biology, 61(12):4711, 2016.

[23] Déte Van Eeden, Freek CP Du Plessis, et al. Multi-energy computed tomography breast imaging with monte carlo simulations: Contrast-to-noise-based image weighting. Journal of Medical Physics, 44(2):106, 2019.

[24] Joscha Maier, Stefan Sawall, Michael Knaup, and Michael Kachelrieß. Deep scatter estimation (dse): Accurate real-time scatter estimation for x-ray ct using a deep convolutional neural network. Journal of Nondestructive Evaluation, pages 27–57, 2018.

[25] B Ohnesorge, T Flohr, and K Klingenbeck-Regn. Efficient object scatter correction algorithm for third and fourth generation CT scanners. European radiology, 9(3): 563–569, 1999.

[26] Katharina Bell, Norbert Licht, Christian Rübe, and Yvonne Dzierma. Image guidance and positioning accuracy in clinical practice: influence of positioning errors and imaging dose on the real dose distribution for head and neck cancer treatment. Radiation Oncology, 13(1), October 2018. doi: 10.1186/s13014-018-1141-8. URL `https://doi.org/10.1186/s13014-018-1141-8`.

[27] S. Fatemi, S. Bortolussi, C. Magni, I. Postuma, M. Bettelli, G. Benassi, N. Zambelli, A. Zappettini, S. Altieri, and N. Protti. Prompt gamma tomography for bnct-spect: a feasibility study using small animal phantoms. In 2018 IEEE Nuclear Science Symposium and Medical Imaging Conference Proceedings (NSS/MIC), pages 1–5, 2018. doi: 10.1109/NSSMIC.2018.8824421.

[28] Ryota Yamauchi, Shingo Tamaki, Yuri Morizane, Sachie Kusaka, Yuichiro Manabe, Yoko Akiyama, Fuminobu Sato, and Isao Murata. Feasibility study on image reconstruction for single-photon emission computed tomography with limited projections by neural networks. Nuclear Instruments and Methods in Physics Research Section A: Accelerators, Spectrometers, Detectors and Associated

Equipment, 986:164700, 2021. ISSN 0168-9002. doi: https://doi.org/10.1016/j.nima.2020.164700. URL https://www.sciencedirect.com/science/article/pii/S0168900220310974.

[29] Minho Kim, Jae Keon Bae, Wonho Lee, and Kyeong Min Kim. Design of gagg based gamma camera for prompt gamma imaging in bnct : Gate simulation study. In 2018 IEEE Nuclear Science Symposium and Medical Imaging Conference Proceedings (NSS/MIC), pages 1–4, 2018. doi: 10.1109/NSSMIC.2018.8824664.

[30] Alexander Winkler. Novel Detector Technologies for Medical Applications at the Example of Tumor Detection in BNCT. Helsingin Yliopisto, first edition, 2017. URL http://urn.fi/URN:ISBN:978-951-51-3692-3.

[31] Jari Kaipio and Erkki Somersalo. Statistical and computational inverse problems, volume 160. Springer Science & Business Media, 2006.

[32] Andrew Gelman, John B. Carlin, Hal S. Stern, David B. Dunson, Aki Vehtari, and Donald B. Rubin. Bayesian Data Analysis. Chapman and Hall/CRC, third edition, 2013.

[33] Ville Kolehmainen, Samuli Siltanen, Seppo Järvenpää, Jari P Kaipio, P Koistinen, M Lassas, J Pirttilä, and E Somersalo. Statistical inversion for medical x-ray tomography with few radiographs: Ii. application to dental radiology. Physics in Medicine & Biology, 48(10):1465, 2003.

[34] Samuli Siltanen, Ville Kolehmainen, Seppo Järvenpää, JP Kaipio, P Koistinen, M Lassas, J Pirttilä, and E Somersalo. Statistical inversion for medical x-ray tomography with few radiographs: I. general theory. Physics in Medicine & Biology, 48(10):1437, 2003.

[35] William H. Sweet. The uses of nuclear disintegration in the diagnosis and treatment of brain tumor. New England Journal of Medicine, 245(23):875–878, December 1951. doi: 10.1056/nejm195112062452301. URL https://doi.org/10.1056/nejm195112062452301.

[36] Sauli Savolainen, Mika Kortesniemi, Marjut Timonen, Vappu Reijonen, Linda Kuusela, Jouni Uusi-Simola, Eero Salli, Hanna Koivunoro, Tiina Seppälä, Nadja Lönnroth, Petteri Välimäki, Heini Hyvönen, Petri Kotiluoto, Tom Serén, Antti Kuronen, Sami Heikkinen, Antti Kosunen, and Iiro Auterinen. Boron neutron capture therapy (BNCT) in finland: Technological and physical prospects after 20 years of experiences. Physica Medica, 29(3):233–248, May 2013. doi: 10.1016/j.ejmp.2012.04.008. URL https://doi.org/10.1016/j.ejmp.2012.04.008.

[37] Rolf F Barth, MGraca H Vicente, Otto K Harling, WS Kiger, Kent J Riley, Peter J Binns, Franz M Wagner, Minoru Suzuki, Teruhito Aihara, Itsuro Kato, and Shinji Kawabata. Current status of boron neutron capture therapy of high grade gliomas and recurrent head and neck cancer. Radiation Oncology, 7(1), August 2012. doi: 10.1186/1748-717x-7-146. URL https://doi.org/10.1186/1748-717x-7-146.

[38] Richard M. Leahy, Bing Bai, and Evren Asma. Physics of PET and SPECT

Imaging, chapter Image reconstruction for PET and SPECT, pages 235–257. CRC press, 2017.

[39] Miles N Wernick and John N. Aarsvold. Emission tomography : the fundamentals of PET and SPECT. Elsevier Academic Press, Amsterdam Boston, 2004. ISBN 0127444823.

[40] Tooru Kobayashi, Yoshinori Sakurai, and Masayori Ishikawa. A noninvasive dose estimation system for clinical BNCT based on PG-SPECT-conceptual study and fundamental experiments using HPGe and CdTe semiconductor detectors. Medical Physics, 27(9):2124–2132, September 2000. doi: 10.1118/1.1288243. URL `https://doi.org/10.1118/1.1288243`.

[41] A. Winkler et al. Prompt gamma and neutron detection in BNCT utilizing a CdTe detector. Appl. Radiat. Isot, 106:139–144, 2015. doi: http://dx.doi.org/10.1016/j.apradiso.2015.07.040.

[42] Stanley Roderick Deans. The Radon transform and some of its applications. Wiley, 1983.

[43] Jennifer L Mueller and Samuli Siltanen. Linear and nonlinear inverse problems with practical applications, volume 10. Siam, 2012.

[44] Tiina Seppälä. FIR 1 Epithermal Neutron Beam Model and Dose Calculation for Treatment Planing in Neutron Capture Therapy. PhD thesis, University of Helsinki, Department of Physical Sciences, Faculty of Science, 2002. URL `http://ethesis.helsinki.fi/julkaisut/mat/fysik/vk/seppala/fir1epit.pdf`.

[45] OECD. OECD Nuclear Energy Agency. https://www.oecd-nea.org, 2016.

[46] Monte Carlo Team. MCNP-A general Monte Carlo N-particle transport code, 2005. Report No. LA-UR-05-8617.

[47] Stephen P Brooks and Gareth O Roberts. Convergence assessment techniques for markov chain monte carlo. Statistics and Computing, 8:319–335, 1998.

[48] Kerrie L Mengersen and Richard L Tweedie. Rates of convergence of the hastings and metropolis algorithms. The annals of Statistics, 24(1):101–121, 1996.

[49] Heikki Haario, Aki Kallonen, Marko Laine, Esa Niemi, Zenith Purisha, and Samuli Siltanen. Shape recovery for sparse-data tomography. Mathematical Methods in the Applied Sciences, 40(18):6649–6669, 2017.